THE JOURNAL OF PHYSICAL CHEMISTRY C
A JOURNAL OF THE AMERICAN CHEMICAL SOCIETY

pubs.acs.org/JPCC

Article

# Intertwined Cross-Scale Structures via Intralayer Anisotropic Fe-Chains in the Layered Ferromagnet $FePd_2Te_2$

Manyu Wang,[⊥] Chang Li,[⊥] Bingxian Shi,[⊥] Shuo Mi, Xiaoxiao Pei, Shumin Meng, Yanyan Geng, Fei Pang, Rui Xu, Li Huang, Wei Ji, Hong-Jun Gao, Peng Cheng,* Le Lei,* and Zhihai Cheng*

Cite This: *J. Phys. Chem. C* 2026, 130, 6653−6662

Read Online

ACCESS | Metrics & More | Article Recommendations | Supporting Information

**ABSTRACT:** Controlling mesoscale and nanoscale material structures and properties through self-organized atomic behavior is essential for atomic-scale manufacturing. However, direct and visual studies of the cross-scale effects of such atomic self-organization on mesoscopic structures remain scarce. Herein, we report the intertwined atomic-nanoscale-mesoscale structures via the intralayer Fe-chains in the sandwich-like layered $FePd_2Te_2$ crystal by scanning tunneling microscopy (STM) and atomic force microscopy (AFM). The hierarchical orthogonal corrugated morphologies are directly revealed and attributed to their chain-orientation-determined twinning-domain effect. Both Fe-chains of the middle-sublayer and two kinds of Te atoms of the top-sublayer are further atomically resolved, indicating the critical effects of Pd atoms/voids on the intralayer anisotropic Fe-chains and the interlayer structural alignment. The thermally induced and strain-related structural transitions of the surface layer are further investigated and discussed based on the proposed filling model of Pd-voids by the intralayer Pd atoms. Our work not only provides a deep understanding of this exotic layered magnetic material but also will inspire more perspectives for tailoring its anisotropic atomic-to-mesoscale structures and properties.

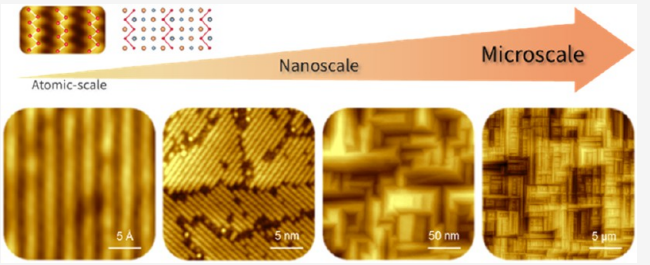




## INTRODUCTION

Two-dimensional (2D) materials have aroused extensive attention since the discovery of graphene.[1−4] Among them, anisotropic 2D material is one kind of 2D materials that possess different properties along different directions caused by anisotropic atoms' arrangement of the 2D materials, mainly including black phosphorus (BP), borophene, and low-symmetry transition-metal dichalcogenides (TMDs).[5−7] This anisotropy may originate from the orientation of the lattice itself, such as in quasi-one-dimensional chain-like structures, or it may arise from more complex atomic structural domains or lattice distortions.[8−11] On this basis, they offer richer and more unique low-dimensional physics compared with isotropic 2D materials.[12−16] Among these, magnetic anisotropy is crucial for stabilizing long-range magnetic order in the two-dimensional limit.[17] Currently, most studied 2D magnets exhibit perpendicular magnetic anisotropy.[18−26] While larger perpendicular magnetic anisotropy allows for high-density information storage devices, two-dimensional magnets with easy-plane magnetic anisotropy are also highly attractive for various spin-related studies and applications. However, 2D magnets with in-plane anisotropy seem to be quite rare, besides $CrCl_3$[27−29] and CrSBr.[30−32]

Recently, a novel quasi-two-dimensional van der Waals material, $FePd_2Te_2$, has been discovered.[33] Its one-dimensional Fe-zigzag chains and strong in-plane easy-axis magnetic anisotropy make $FePd_2Te_2$ a unique material platform for studying both low-dimensional magnetism and spintronic applications. Anisotropic magnetoresistance was performed to investigate the twin-induced in-plane anisotropy, and 4-fold symmetry was discovered. The Hopkinson effect observed in both AC and DC magnetic susceptibility indicates intense magnetic domain motion, which is rather rare in other van der Waals ferromagnets.[34] $FePd_2Te_2$ exhibits pronounced zero-field anomalous Hall effect (AHE) and anomalous Nernst effect (ANE) below $T_C$ (183 K), making it a promising candidate material for practical thermoelectric spintronics applications.[39] It is noteworthy that studies reporting this compound indicate that the magnetic anisotropy of $FePd_2Te_2$ crystals is associated with significant twinning phenomena at the submicron scale,[35−40] which is closely related to the one-dimensional Fe-chains at the atomic scale. Consequently, $FePd_2Te_2$ provides a suitable platform for achieving controlled cross-scale interplay of structure and properties at the atomic level.

**Received:** January 30, 2026
**Revised:** April 15, 2026
**Accepted:** April 16, 2026
**Published:** April 22, 2026

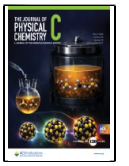

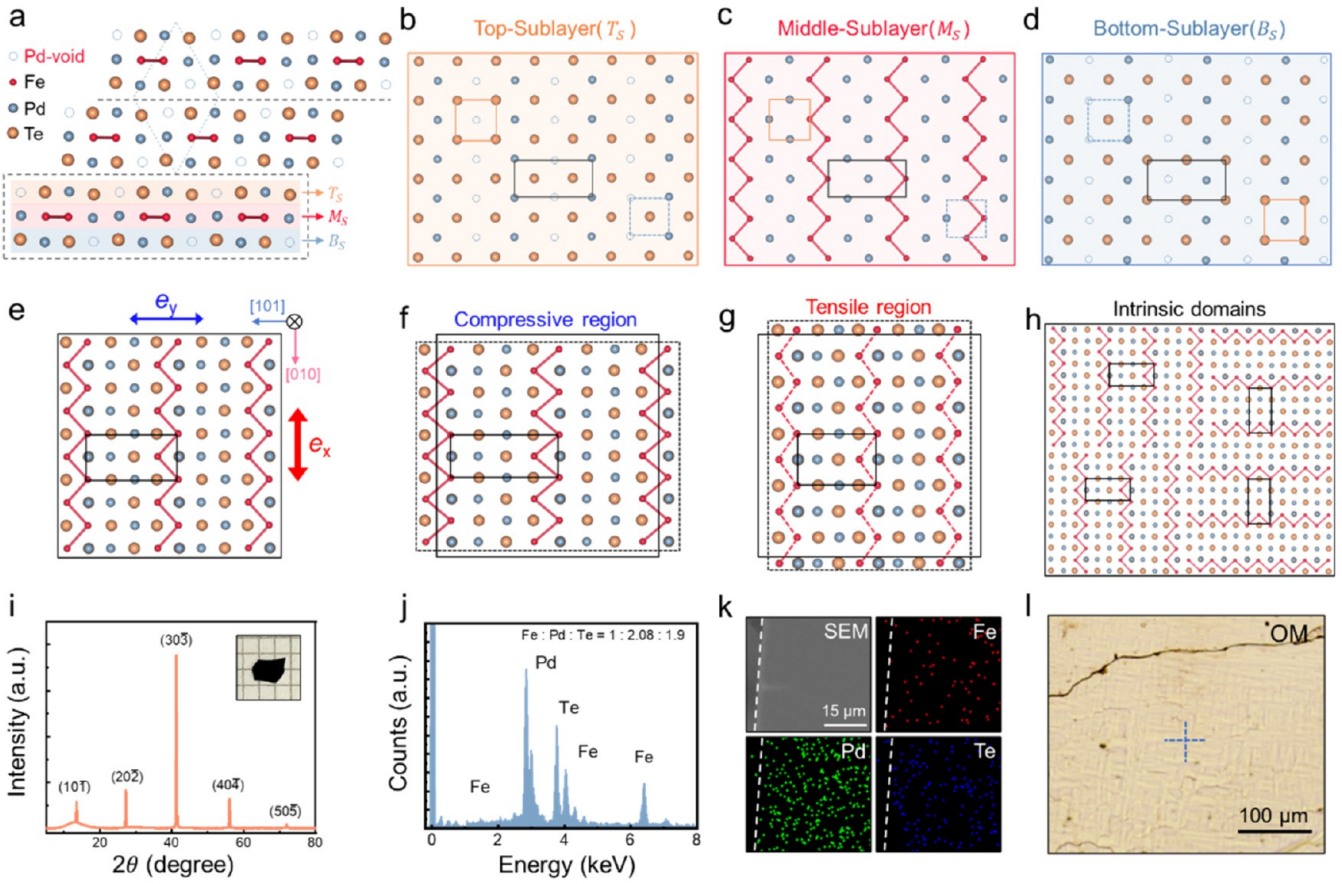


**Figure 1.** Crystal structure of sandwich-like layered $FePd_2Te_2$. (a) Side view of the atomic structure of $FePd_2Te_2$. The crystal structure shows a layered structure along the $[10\bar{1}]$ directions. The crystal can be easily exfoliated between the $Pd_{0.5}Te$ sublayers, as indicated by the black dashed lines. (b–d) Top view of the top-sublayer (b, $Pd_{1/2}Te$), middle-sublayer (c, FePd), and bottom-sublayer (d, $Pd_{1/2}Te$) for the sandwich-like layer of $FePd_2Te_2$. (e) Top view of the atomic structure of $FePd_2Te_2$. The Fe-zigzag chains lie in the exfoliation $(10\bar{1})$ plane and along the [010] directions, contributing anisotropic mechanical properties with large ($e_x$, along the chain) and small ($e_y$, vertical to the chain) Young's modulus. (f, g) Schematics of the compressive (f) and tensile (g) regions after structural relaxation from the unstressed layers of (e) due to their distributed anisotropic domains. "Compressive" and "tensile" refer to lattice distortions along the direction of the Fe-chains. The red dashed lines in (g) highlight regions where the Fe-chains appear disrupted. (h) Schematic diagram of the coexistence of two kinds of intrinsic domains with the orientation-domain (O-domain) and the phase-domain (P-domain). (i) XRD patterns from the cleavage plane of a $FePd_2Te_2$ single crystal. (j, k) EDS elemental analysis (j) and corresponding mapping (k) of one exfoliated flake. (l) Optical microscopy with orthogonal corrugated characteristics of $FePd_2Te_2$.

In this work, we systematically report and dissect the intertwined atomic-nanoscale-mesoscale structures that emerge from the intralayer anisotropic Fe-chains within the sandwich-like layered ferromagnet $FePd_2Te_2$. By combining scanning tunneling microscopy (STM) and atomic force microscopy (AFM), we directly visualize the hierarchical orthogonal corrugated morphologies from the mesoscale to the atomic scale. These unique morphologies arise from a self-organized twinning mechanism governed by an Fe-chain orientation. At the atomic scale, our STM results achieve resolving the Fe-zigzag chains of the middle-sublayer and the two kinds of Te atoms of the top-sublayer. This indicates the critical effects of Pd atoms/voids on the intralayer anisotropic Fe-chains and the interlayer structural alignment. We further probe thermal- and strain-induced structural transitions of the surface layer, proposing a filling model of Pd-voids by intralayer Pd atoms to explain the evolution. This work establishes a foundational framework for rationally designing and controlling its anisotropic structures and associated properties across atomic- to mesoscale dimensions.

## MATERIALS AND METHODS

### Sample Preparation and Characterization

Single crystals of $FePd_2Te_2$ were grown by melting stoichiometric elements. Iron, palladium, and tellurium powder were mixed and ground in a molar ratio of 1:2:2. Deviation from this ratio would lead to the unsuccessful growth of large single crystals or a target phase. Then the mixtures were placed in an alumina crucible and sealed in a quartz tube under vacuum conditions. The entire tube was heated in a box furnace to 800 °C and held at that temperature for 2 days. Then it was cooled to 600 °C at a rate of 2 °C/h, followed by annealing at this temperature for 2 days before being furnace-cooled to room temperature. In addition, we found that quenching the samples at 600 °C would improve the crystal quality, as revealed by X-ray characterization. However, direct quenching in the initial growth process seems to break the large crystal into small pieces. By reannealing and quenching the large single crystal grown by the initial furnace-cooled method, one could obtain crystals with both large size and good quality.

### Structure and Composition Characterization

The structure of $FePd_2Te_2$ crystals was analyzed at 273 K by X-ray diffraction (XRD) (D8 ADVANCE, Bruker) equipped with a multilayer mirror monochromatized Mo K$\alpha$ ($\lambda$ = 0.71073 Å)



https://doi.org/10.1021/acs.jpcc.6c00663
J. Phys. Chem. C 2026, 130, 6653−6662

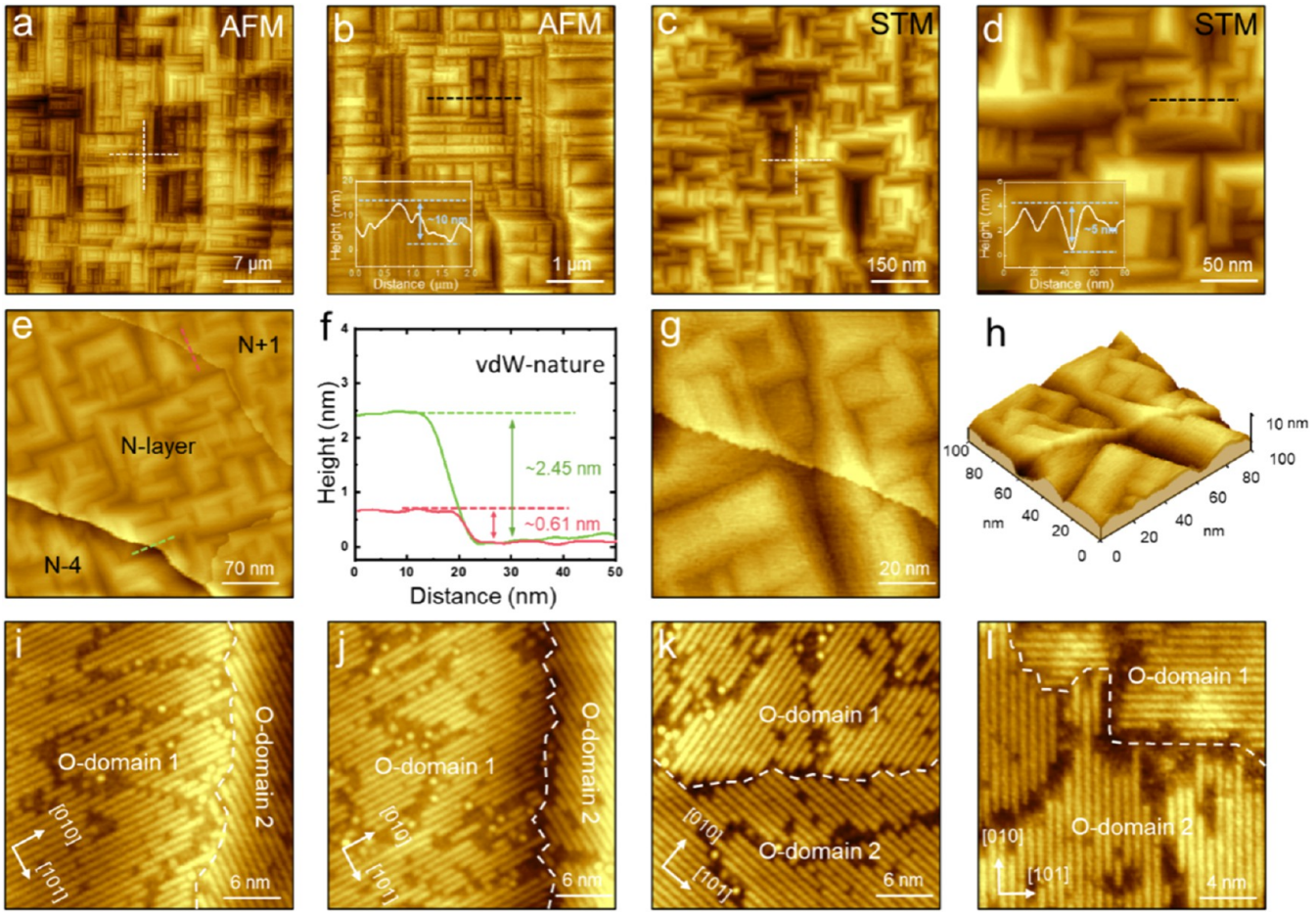


**Figure 2.** Microscale AFM and nanoscale STM measurements of $FePd_2Te_2$. (a) Micrometer-scale AFM topography of the freshly cleaved crystal with orthogonal characteristics. (b) Typical AFM topography of the mesoscale orthogonal corrugated regions. Inset: Line profile along the black dashed line in (b) with vertical heights of ~10 nm. (c) Nanometer-scale STM image with orthogonal characteristics. (d) Typical STM image of the nanoscale orthogonal corrugated domains. Inset: Line profile along the dashed line in (d) with vertical heights of ~5 nm. (e,f) Typical STM image (e) and height line profiles (f) for the surface step edges, demonstrating the 2D-layered nature of the corrugated crystal. (g, h) 2D- (g) and 3D-view (h) of STM image with a single-layer step edge. (i–l) STM images of O-domains with the ridge (i), valley (j, k), and flat (l) boundaries, which are highlighted by the white dashed lines. Scanning parameters: (c, d) $V_s = -0.2$ V, $I_t = -100$ pA; (e, g) $V_s = -0.6$ V, $I_t = -200$ pA; (i–l) $V_s = -0.3$ V, $I_t = -200$ pA.

radiation. The elemental composition and distribution were evaluated by EDS (X-MaxN 50 $mm^2$, Oxford Instruments) in the scanning electron microscope (SEM).

### AFM Measurements

The AFM experiments were performed using a commercial atomic force microscope (Park, NX10) equipped with a commercial topography tip (Nanosensors, AC160TS, Quality factor ~500 at room temperature). The scanning probe system was operated at the resonance frequency of the topography tip, ~301 kHz. The AFM images were acquired in noncontact mode.

### STM and nc-AFM Measurements

High-quality $FePd_2Te_2$ crystals were cleaved at room temperature in ultrahigh vacuum at a base pressure of $2 \times 10^{-10}$ Torr and directly transferred to the cryogen-free variable-temperature STM system (PanScan Freedom, RHK). Chemically etched Pt–Ir tips were used for the STM measurement in constant current mode. The tips were calibrated on a clean Ag(111) surface. Gwyddion was used for the STM data analysis. $FePd_2Te_2$ crystals were cleaved at liquid nitrogen temperature in ultrahigh vacuum. The nc-AFM measurements were performed in a commercial LT-STM system (LT-STM/AFM, CreaTec) equipped with an STM/qPlus sensor at 4.5K. The nc-AFM images were recorded by measuring the frequency shift of the qPlus resonator (sensor frequency $f_0$ = 30 kHz, $Q$ = 53000) in constant-height mode with an oscillation amplitude of 200 pm.

## RESULTS

Figure 1a shows the anisotropic crystal structure of $FePd_2Te_2$, which is in monoclinic $P21/m$ symmetry with refined unit-cell parameters $a = 7.5024(5)$ Å, $b = 3.9534(2)$ Å, $c = 7.7366$[7] Å, $\alpha = \gamma = 90°$, and $\beta = 118.15°$, consistent with previous single-crystal XRD refinement results.[30] As an atypical layered material, its cleavage interface (marked by dashed lines) occurs along the $(10\bar{1})$ plane between the sandwich-like layers. As shown in Figure 1b–d, each sandwich-like layer of $FePd_2Te_2$ is made of top-sublayer ($T_s$, $Pd_{1/2}Te$), middle-sublayer ($M_s$, FePd), and bottom-sublayer ($B_s$, $Pd_{1/2}Te$), in which the intersublayer alignments of atoms are marked by the squares and rectangles. The anisotropic Fe-zigzag chains are confined by the Pd atoms within the middle-sublayer and further sandwiched between the top- and bottom-sublayers. It is noted that the $Pd_{1/2}Te$-sublayers could be assumed as the PdTe-sublayers with the Pd-voids (marked by open circles) in the high-symmetric structure. The formation of Pd-voids in the PdTe-sublayer can be understood as the position-shifting of Pd



https://doi.org/10.1021/acs.jpcc.6c00663
J. Phys. Chem. C 2026, 130, 6653–6662

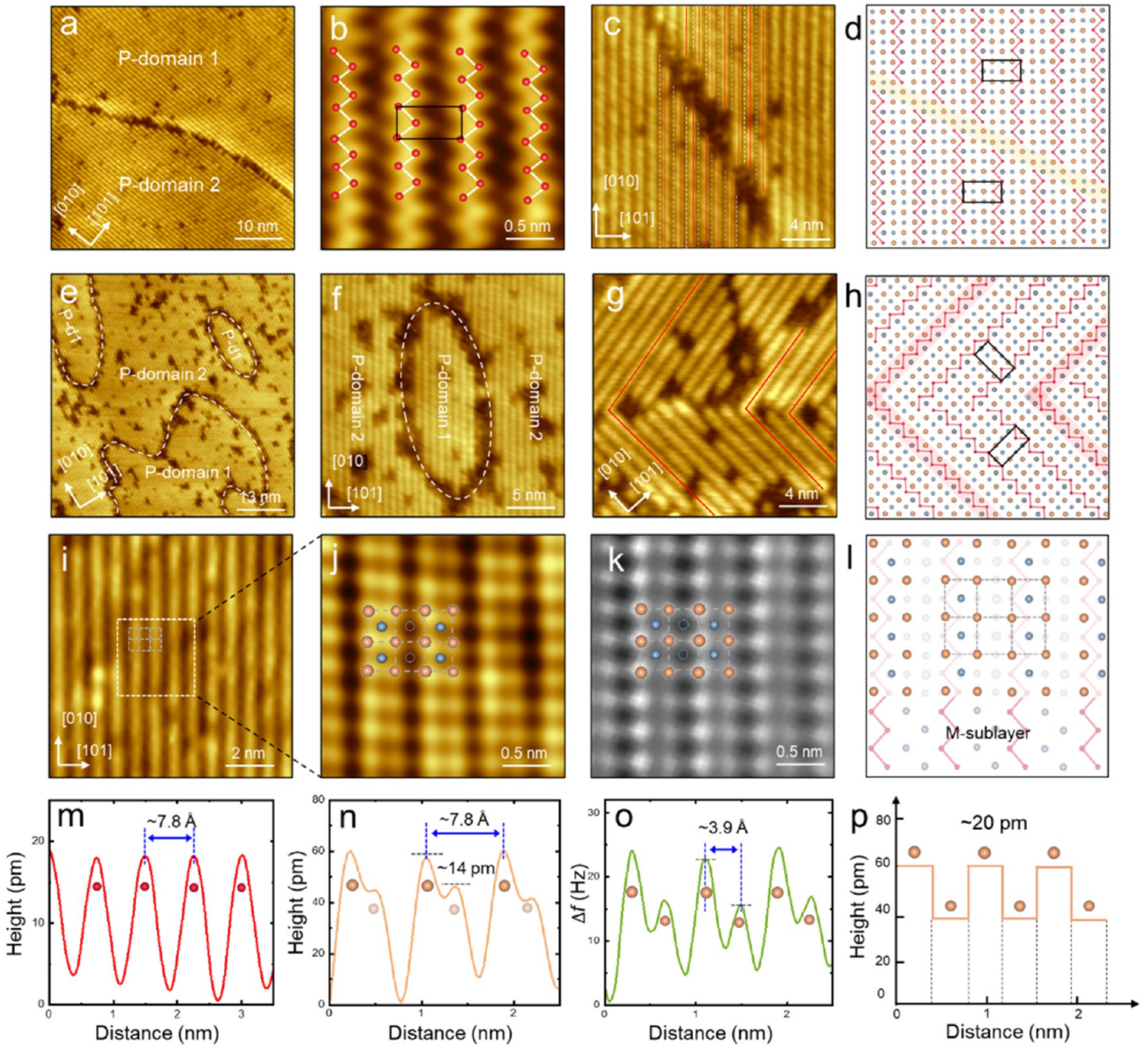


**Figure 3.** Phase-domain and atomic-scale structures of the intact $FePd_2Te_2$ layer. (a) STM image of the pristine surface with a single O-domain made of two P-domains. (b) High-resolution STM image of Fe-zigzag chains with its overlaid model. (c, d) STM image of the two P-domains (c) and its schematic model (d) with the broken boundary. (e, f) Large-scale (e) and zoom-in (f) STM images of the P-domains with the highlighted boundaries. (g,h) High-resolution STM image of the O-domain boundary (g) and its schematic model (h). (i, m) High-resolution STM image (i) and line profile of the Fe-chains (m). (j, n) Atomic-resolution STM image (j) and line profile (n) of the top-$Pd_{1/2}Te$-sublayer, exhibiting two kinds of Te atoms with slight apparent height difference. (k,o) Atomic-resolution nc-AFM image (k) and line profile of the Te atoms (o) in the top-$Pd_{1/2}Te$-sublayer. (l) Schematic model of the top-$Pd_{1/2}Te$-sublayer (top-panel) and middle-FePd-sublayer (bottom-panel). (p) Schematic height profile of the Te atoms within the top-sublayer. Scanning parameters: (a, i) $V_s = -0.3$ V, $I_t = -200$ pA; (b, j) $V_s = -0.7$ V, $I_t = -140$ pA; (c) $V_s = -0.7$ V, $I_t = -200$ pA; (e−g) $V_s = -0.5$ V, $I_t = -100$ pA.

atoms from the top- and bottom-sublayers to the middle-sublayer, which plays important roles in the formation of Fe-chains and the relatively strong interface bonding, as shown in the proposed schematic models in Figure S1.

The in-plane unit-cell of $FePd_2Te_2$ layers is marked by the solid rectangle in their top-view structural model of Figure 1e, demonstrating the Fe-chain-induced anisotropic structures. The atomic bonding is expected to be stronger along the chains ($e_x$, parallel to the [010] direction) and weaker between the chains, leading to the relatively large and small Young's modulus, respectively, as illustrated in Figure 1e. Considering their anisotropic Young's modulus, the formation of compressive ($C$) and tensile ($T$) regions could occur under the internal strains after structural relaxations of spatially distributed domains (Figures 1h and S2), as shown in Figure 1f,1g. The twinning-like orientation-domains (O-domains) originate from the low-symmetric anisotropic Fe-chains (middle-sublayer) and the quasi-high-symmetric PdTe (top-/bottom-sublayer), as shown in Figure 1h. While another kind of charge density wave-like (CDW-like) phase-domain (P-domain) derives from the large quasi-supercell of Fe-chains with respect to the small quasi-cell of PdTe-sublayer,



https://doi.org/10.1021/acs.jpcc.6c00663
J. Phys. Chem. C 2026, 130, 6653−6662

highlighted by the marked rectangles in Figure 1h. It is noted that these intrinsic domains are structurally equivalent and energetically degenerate, and should coexist within the synthesized bulk crystals. Both O-domains and P-domains exhibit domain boundaries at different angles, as illustrated in the structural models in Figures S3 and S4, which contribute to complex structure, morphology, and properties.

$FePd_2Te_2$ exhibits metallic behavior. The single-crystal samples were grown by melting stoichiometric elements and characterized by X-ray diffraction (XRD) and energy dispersive spectroscopy (EDS).[30] By performing XRD measurements on the cleavage plane of $(10\bar{1})$, the Bragg peaks are indexed as $(H0\bar{H})$, as shown in Figure 1i, with an inset photo of a typical crystal. Further EDS elemental analysis (Figure 1j) and mapping characterizations (Figure 1k) confirm the chemical composition of $FePd_2Te_2$ with a uniform spatial distribution. The optical microscope image of a typical crystal sample is given in Figure 1l, which clearly displays impressive orthogonal characteristics on a tens of micrometer scale, clearly different from the known isotropic or anisotropic 2D materials. Notley, these distinct mesoscale features are highly reproducible across multiple samples and cleaved flakes and should intrinsically originate from its sandwich-like layered atomic structures via the anisotropic Fe-chains between the quasi-symmetric PdTe-sublayers. As we will demonstrate in the following STM and AFM results (Figures 2 and 3), these atomic-scale features (Fe-zigzag chains and Pd-voids) are directly responsible for the formation of O-domains and P-domains, ultimately giving rise to the orthogonal corrugated morphologies observed at the nanoscale and microscale.

Figure 2a,2b presents the large-scale and zoomed-in AFM topography of the fresh-cleaved $FePd_2Te_2$ surface, in which the complex orthogonal (marked by the dashed cross) and corrugated (shown by the line profile) morphologies are directly resolved at the micrometer scale and consistent with the optical characterizations. Figure 2c,d presents the typical large-scale and high-resolution STM topography images, in which similar orthogonal and corrugated features are also observed at the nanometer scale. It is clear that the above-observed orthogonal features are self-similar hierarchical cross nanoscale-to-microscale, which is never observed in 2D-layered materials but occasionally occurs in specific 3D bulk materials according to our knowledge. Additional AFM and STM images from multiple cleaved flakes and distinct samples are presented in Figure S5, confirming the high reproducibility of these features across different samples.

Even with the prominent surface corrugations, the layered nature of $FePd_2Te_2$ as atypical 2D materials still can be clearly identified by the distinct single- and four-layer step edges, as shown in Figure 2e,2f. It has been confirmed that van der Waals-like stratification of the crystal. The determined thickness of the single layer is ~0.6 nm, consistent with the XRD-determined structural model. The high-resolution 2D- and 3D-view STM images with the step edge, as shown in Figure 2g,2h, directly indicate the continuity of surface corrugations across the step edges. It is clear that the corrugations of each layer are consistent and transfer through their strong interlayer bonding. More STM images (Figure S6) further confirm the consistency of the corrugations of each layer. This observation is critical, as it demonstrates that the complex orthogonal and corrugated morphology is not an artifact confined to a single-layer terrace or a result of local reconstruction.

Figure 2i,2j shows the atomic-scale STM images for the typical ridges and valleys areas of the mountain-like corrugations, in which the chain-like structures are clearly resolved. The marked ridge- and valley-domain walls separate the two stitched O-domains with orthogonal chains. The FFT and Fourier-filtered images of the O-domain (Figure S7) further confirm the orthogonality of the Fe-chains. It is consistent with our proposed model for the structural relaxations due to the anisotropic mechanical properties (Figure S8). Another two kinds of O-domain walls are also shown in Figure 2k,2l with tiny and negligible valley- and ridge-corrugations. Most O-domain boundaries are along the valley or ridges of surface corrugations, demonstrating the intertwined atomic structures, nanoscale domains, and micro-scale morphology via the anisotropic Fe-chains.

Based on its specific crystal structure shown in Figure 1, it is inferred that the CDW-like phase-domains (P-domain) will also exist and should be observed in the STM images of $FePd_2Te_2$. Different from the large corrugated O-domains, the P-domains are only found within the O-domains, as shown in Figure 3a, in which two P-domains coexist within a single O-domain. The higher-resolution STM image in Figure 3b directly shows the zigzag structure of Fe-chains within the middle-sublayer of $FePd_2Te_2$. A zoomed-in STM image of the P-domain boundary is presented in Figure 3c, in which the Fe-chains are marked with red solid lines and separated by the white dashed lines. This clearly shows that the Fe-chains of P-domains shift one Te atomic period across the P-domain boundary, as schematically shown in the structural model in Figure 3d. This shift originates from the large quasi-supercell of Fe-chains with respect to the small quasi-cell of the PdTe-sublayer, as illustrated in Figure 1h. It is noted that the Fe-chains are completely disconnected at the P-domain boundary. This finding is also corroborated by the observed P-domain boundary marked with white dashed lines in both the larger-scale (Figure 3e) and the zoomed-in (Figure 3f) P-domain STM images.

Meanwhile, unlike the corrugated O-domain in Figure 2a, the P-domains exhibit no significant vertical height difference (Figure S9). As shown in Figure S10, the anisotropic Fe-chains contribute to the different mechanical properties (Young's modulus) across the boundary of the O-domain but not across the boundary of the P-domains. Due to the absence of internal strain, no corrugated regions are formed across the P-domain boundaries during the structural relaxation, indicating the difference between P-domains and O-domains. Furthermore, the distinction between the two domains also lies in the Fe-chains at their boundary. The STM image of the zoomed-in image of the O-domain (Figure 3g) clearly shows that some Fe-chains can directly connect and rotate by 90° (highlighted by red solid lines) across the O-domain boundary. The corresponding structural model is presented in Figure 3h. Through direct visual comparison of the STM images in Figures 2 and 3, the distinct characteristics of the two domain types—particularly in terms of boundary topography and Fe-chains configuration.

The existence of these two kinds of domain structures relies entirely on the unique Fe-chain structures of $FePd_2Te_2$. Next, we further conducted atomic-resolution studies of the surface layer. Figure 3i,3m displays high-resolution STM images and line profiles of the Fe-chains, in which the Fe-chains appear as parallel bright lines with uniform distribution and consistent height. Figure 3j,3n shows its corresponding atomic-resolution


https://doi.org/10.1021/acs.jpcc.6c00663
J. Phys. Chem. C 2026, 130, 6653−6662

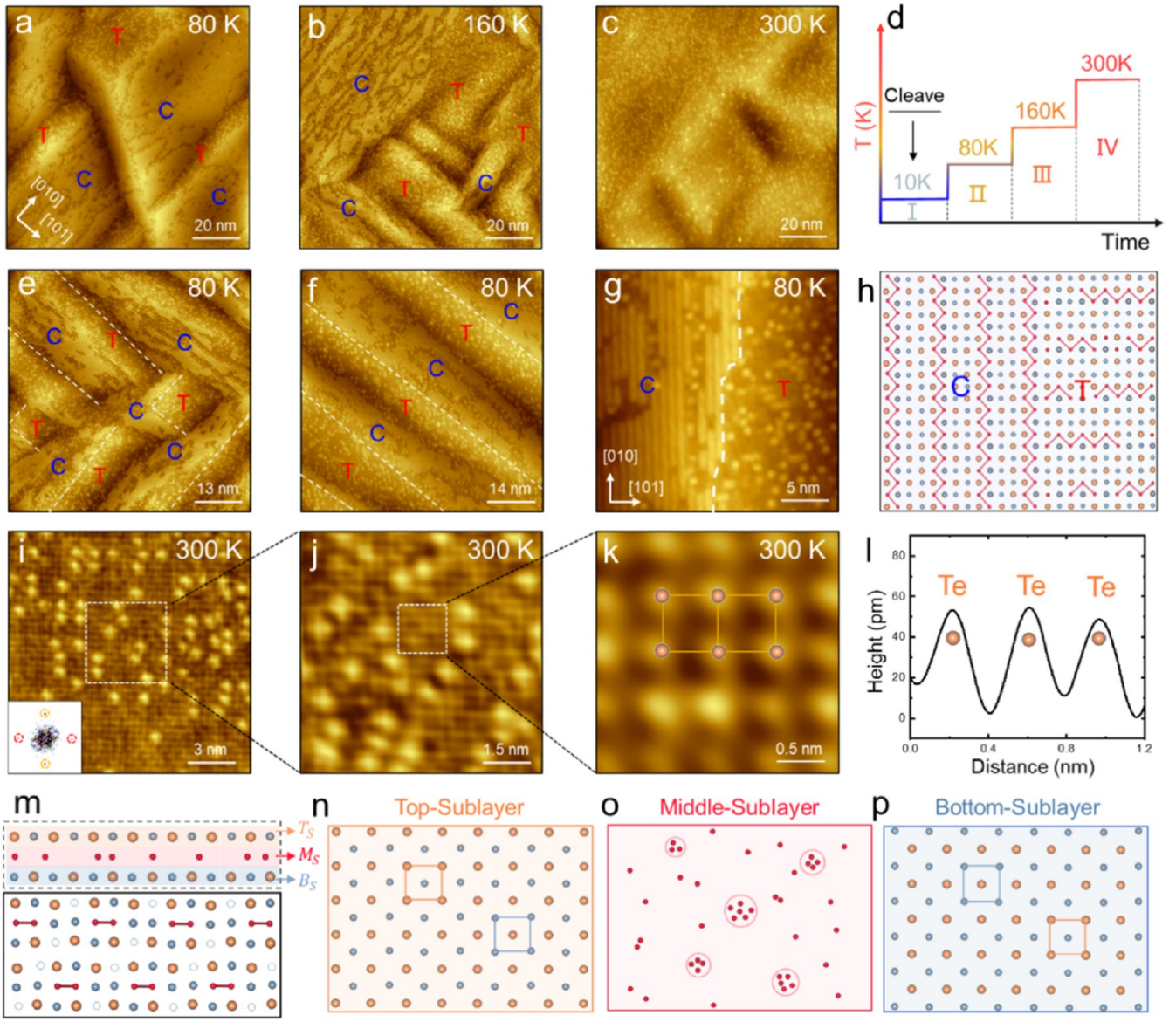


**Figure 4.** Temperature-dependent structural transitions of the $FePd_2Te_2$ surface layer. (a–d) STM images of the surface layer at Stage II (a, ~80 K), Stage III (b, ~160 K), and Stage IV (c, ~300 K) from the initial intact Stage I (Figure 3a, ~10 K), sequentially obtained during the schematic procedure (d). (e,f) STM images at Stage II (~80 K) of the C and T regions with higher and lower stabilities, indicated by their relatively intact and broken Fe-chains, respectively. (g, h) High-resolution STM image (g) at Stage II (~80 K) and schematic model (h) for the intact and broken Fe-chains at the C and T regions. (i, j) Large-scale (i) and high-resolution (j) STM images at Stage IV (~300 K) of the surface layer after thermal-induced structural transition, in which the relative uniform Te atoms and bright spots (possible Fe atoms/clusters) are resolved. (k, l) Atomic-resolution STM image (k) at Stage IV (~300 K) and line profile (l) of the top-sublayer Te atoms, different from Figure 3j. (m–p) Proposed schematic models of the surface layer (m) after structural transition and its top-sublayer (n, PdTe), middle-sublayer (o, Fe atoms/clusters), and bottom-sublayer (p, PdTe). Scanning parameters: (a–c) $V_s$ = −0.5 V, $I_t$ = −100 pA; (e–g) $V_s$ = −0.2 V, $I_t$ = −200 pA; (i–k) $V_s$ = −0.1 V, $I_t$ = −200 pA.

STM images and line profiles of the top-$Pd_{1/2}Te$ sublayer, in which two kinds of Te atoms are observed with a slight apparent height difference. This is consistent with the atomic structure diagram in Figure 1a and directly shown with the overlaid model in Figure 3j. Furthermore, the atomic-resolution nc-AFM image (Figure 3k) and the line profile of Te atoms (Figure 3o) provide additional confirmation of the slight height difference between the Te atoms. It should be noted that the STM image in Figure 3j reflects a convolution of the surface geometry and local electronic states. Therefore, the measured spacing between adjacent Te atoms may not correspond strictly to the real atomic distance. A schematic model of the top-$Pd_{1/2}Te$ sublayer and middle-FePd sublayer is depicted in Figure 3l. The Te atoms in the top-$Pd_{1/2}Te$-sublayer are marked with dashed squares, and the Pd atoms and Pd-voids of the top-sublayer are also resolved and marked with the blue balls and empty circles. It is also noted that the slight height difference of the Te atoms represents the underlying respective Fe-chains and Pd atoms within the middle-FePd-sublayer. Figure 3p displays the schematic height profile of the Te atoms within the top-sublayer, illustrating the unique characteristics of Te atoms in the $Pd_{1/2}Te$-sublayer.

Due to the anisotropic Young's modulus, the formation of compressive (C) and tensile (T) regions can occur under the



https://doi.org/10.1021/acs.jpcc.6c00663
J. Phys. Chem. C 2026, 130, 6653−6662

inherent internal strains, which is related to the corrugated O-domains. After the low-temperature cleavage, the $FePd_2Te_2$ samples can sequentially undergo four different distinct stages (Figure 4d). At Stage I (~10 K, directly after low-temperature cleaving), as shown in the STM images of Figures 2 and 3, all of the O-domains show the intact Fe-chains. With the increased sample temperature at ~80 K (Stage II), only partial corrugated regions (marked by red **T**) show the decomposed Fe-chains as the distributed bright spots in the STM images (Figure 4a). At Stage III (~160 K), the Fe-chains in the remaining regions (marked by blue **C**) also gradually decomposed (Figure 4b). At Stage IV (~300 K), all of the Fe-chains completely decomposed into the distributed bright spots. The specific thermal stability of different regions should be related to their internal strain conditions. Figure 4e,f displays the typical STM images at Stage II; the intertwined C and T domains clearly display the intact and decomposed Fe-chains, respectively, indicating their higher and lower thermal stabilities. Figure 4g,4f shows the high-resolution STM image and schematic model for the intact and decomposed Fe-chains at the C and T regions. This temperature-dependent structural transition occurs exclusively at the surface layer, and the underlying layers retain their intact structures (Figures S11 and S12).

The temperature-dependent structural transition at the surface layers is irreversible: once the Fe-chains have decomposed upon heating, they do not recover upon cooling. This irreversibility enables the transformed structure with decomposed Fe-chains to be preserved and atomically investigated (Figure S14). Figure 4i,j shows large-scale and high-resolution STM images of the surface layer after the thermally induced structural transition. It is clear that no pristine parallel chains but the randomly distributed bright spots (possible Fe atoms/clusters) are observed with the uniform Te atoms in the square configuration. The zoomed-in STM images reveal the atomic-resolution image (Figure 4k) and line profile (Figure 4l) of the top-sublayer Te atoms. Different from Figure 3j, the top-sublayer Te atoms exhibit a relatively uniform height after the structural transition. The proposed structural model of the surface layer after the transition is schematically displayed in Figure 4m, and detailed structural transition processes are schematically shown in Figure S13. After the cleavage, the decreased interlayer interactions of the surface layer weaken its intralayer structural stabilities. With the thermal energies, the Pd atoms of the middle-sublayer can be shifted to fill the Pd-voids at the top- and bottom-sublayers to form the stable top- and bottom-PdTe-sublayers (Figure 4n,p). The remaining Fe-chains within the middle-sublayer are structurally unstable without the confinement effect of Fe-chains and gradually decomposed into disordered Fe atoms/clusters (Figure 4o) confined between the well-structured top- and bottom-PdTe-sublayers. By comparing the structural models before and after the transition (Figure S15), we can conclude that the unique shifting of Pd atoms/voids among the sandwich-like sublayers plays a critical role in the formation of intralayer anisotropic Fe-chains and the interlayer structural alignment via the strong interlayer bonding.

## DISCUSSION

This work demonstrates that the unique structure of the layered ferromagnet $FePd_2Te_2$ is fundamentally determined by the arrangement of Pd atoms and voids. At the atomic scale, these Pd atoms and voids exert a critical influence on the two kinds of Te atoms in the top-sublayer and the anisotropic 1D Fe-chains in the middle-sublayer, thereby controlling interlayer interactions. This atomic order dictates the formation of nanoscale self-organized domains driven by a chain-orientation-dependent mechanical coupling effect. Ultimately, these domains assemble into orthorhombic corrugated morphologies at the mesoscale. Through combined scanning tunneling microscopy and atomic force microscopy observations, we directly visualized this cross-scale correlation, revealing how local atomic arrangements dictate structural order at both the nanoscale and the mesoscale. Furthermore, we observe intriguing strain- and temperature-dependent reconstruction of the surface layer. The atoms in the surface sandwich layer keep long-range ordered 4-fold symmetry in the top- and bottom-sublayers, while in contrast, the Fe atoms in the middle-sublayer form a completely disordered cluster-like structure. The discovery of this unique order−disorder stacking structure and its formation process provides insights and new strategies in engineering 2D materials at the atomic scale.

Penacchio et al. reported the bulk $FePd_2Te_2$ has a structure phase transition near 420 K and might form a new crystal structure with 4-fold symmetry, but the detailed crystal structure is unresolved.[37] The order−disorder stacking surface structure discovered in this work also has 4-fold symmetry and tends to form at higher temperatures, similar to our experimental structure. This indirectly confirms the validity of our filling model. So, an interesting speculation is that this surface structural modulation may extend to the whole bulk near 420 K. If so, new opportunities in modulating the atoms in the bulk near room temperature will be provided. Ruiz et al. reported that substitution atoms of Co and Ni can effectively modulate the exchange coupling and anisotropy properties of $FePd_2Te_2$ through DFT calculations.[40] Mechanical strain serves as an effective means to regulate the magnetic properties of $FePd_2Te_2$ and $CoPd_2Te_2$, providing theoretical support for designing spintronic devices with customized magnetism through chemical and structural manipulation. This work further reveals that the distribution and occupancy of Pd atoms/voids are key factors determining the 1D Fe-chain structure and orthorhombic domain morphology. Based on this, we propose that methods such as atomic intercalation to alter van der Waals interlayer spacing, quenching treatment, element substitution, and designing specific element ratios can effectively regulate Pd atoms/voids arrangement and content, thereby directly influencing Fe-chain configuration and domains. This potentially provides a clear physical picture and a feasible material design platform for achieving fine-tuned control of magnetic anisotropy experimentally.

## CONCLUSIONS

Combined STM/AFM data directly confirm that the unique hierarchical structure of $FePd_2Te_2$ originates from the atomic-scale configuration of Pd atoms/voids. This arrangement simultaneously regulates the two kinds of Te atoms and anisotropic Fe-chains, thereby driving the self-assembly of nanoscale domains and ultimately forming an orthorhombic corrugated morphology at the mesoscale. Furthermore, we observe a unique coexistence of ordered and disordered phases in the surface layers: top-/bottom-sublayers consist of ordered PdTe-sublayers, intercalated with disordered Fe-sublayers. This distinctive stacking structure arises from its evolution


https://doi.org/10.1021/acs.jpcc.6c00663
J. Phys. Chem. C 2026, 130, 6653−6662

with strain and temperature. Our work reveals the cross-scale intertwining of intrinsic structural anisotropy in a layered ferromagnet, establishing a fundamental framework for understanding structure−property relationships in anisotropic two-dimensional materials.

## ■ ASSOCIATED CONTENT

### Data Availability Statement

The authors declare that the data supporting the findings of this study are available within the article and its Supporting Information.

### Supporting Information

The Supporting Information is available free of charge at https://pubs.acs.org/doi/10.1021/acs.jpcc.6c00663.

Schematic diagrams illustrating the proposed structural transition mechanism, intrinsic domain structures (O-domains and P-domains), and their boundary configurations; additional AFM and STM topography images from multiple samples, FFT analysis of O-domains, STM images of P-domains under different bias conditions; schematic diagrams of the cleaved $FePd_2Te_2$, the temperature-dependent structural evolution, including C/T domain behavior, and comparative structural models before and after transition (PDF)

## ■ AUTHOR INFORMATION


### Corresponding Authors

**Peng Cheng** − *Key Laboratory of Quantum State Construction and Manipulation (Ministry of Education), School of Physics, Renmin University of China, Beijing 100872, China; Beijing Key Laboratory of Optoelectronic Functional Materials & Micro-Nano Devices, School of Physics, Renmin University of China, Beijing 100872, China;* orcid.org/0000-0003-2351-2060; Email: pcheng@ruc.edu.cn

**Le Lei** − *Institute of Quantum Materials and Physics, Henan Academy of Sciences, Zhengzhou 450046, China;* Email: lelei@hnas.ac.cn

**Zhihai Cheng** − *Key Laboratory of Quantum State Construction and Manipulation (Ministry of Education), School of Physics, Renmin University of China, Beijing 100872, China; Beijing Key Laboratory of Optoelectronic Functional Materials & Micro-Nano Devices, School of Physics, Renmin University of China, Beijing 100872, China;* orcid.org/0000-0003-4938-4490; Email: zhihaicheng@ruc.edu.cn

### Authors

**Manyu Wang** − *Key Laboratory of Quantum State Construction and Manipulation (Ministry of Education), School of Physics, Renmin University of China, Beijing 100872, China; Beijing Key Laboratory of Optoelectronic Functional Materials & Micro-Nano Devices, School of Physics, Renmin University of China, Beijing 100872, China*

**Chang Li** − *Key Laboratory of Quantum State Construction and Manipulation (Ministry of Education), School of Physics, Renmin University of China, Beijing 100872, China; Beijing Key Laboratory of Optoelectronic Functional Materials & Micro-Nano Devices, School of Physics, Renmin University of China, Beijing 100872, China*

**Bingxian Shi** − *Key Laboratory of Quantum State Construction and Manipulation (Ministry of Education), School of Physics, Renmin University of China, Beijing 100872, China; Beijing Key Laboratory of Optoelectronic Functional Materials & Micro-Nano Devices, School of Physics, Renmin University of China, Beijing 100872, China*

**Shuo Mi** − *Key Laboratory of Quantum State Construction and Manipulation (Ministry of Education), School of Physics, Renmin University of China, Beijing 100872, China; Beijing Key Laboratory of Optoelectronic Functional Materials & Micro-Nano Devices, School of Physics, Renmin University of China, Beijing 100872, China*

**Xiaoxiao Pei** − *Beijing National Laboratory for Condensed Matter Physics, Institute of Physics, Chinese Academy of Sciences, Beijing 100190, China*

**Shumin Meng** − *Key Laboratory of Quantum State Construction and Manipulation (Ministry of Education), School of Physics, Renmin University of China, Beijing 100872, China; Beijing Key Laboratory of Optoelectronic Functional Materials & Micro-Nano Devices, School of Physics, Renmin University of China, Beijing 100872, China*

**Yanyan Geng** − *Key Laboratory of Quantum State Construction and Manipulation (Ministry of Education), School of Physics, Renmin University of China, Beijing 100872, China; Beijing Key Laboratory of Optoelectronic Functional Materials & Micro-Nano Devices, School of Physics, Renmin University of China, Beijing 100872, China*

**Fei Pang** − *Key Laboratory of Quantum State Construction and Manipulation (Ministry of Education), School of Physics, Renmin University of China, Beijing 100872, China; Beijing Key Laboratory of Optoelectronic Functional Materials & Micro-Nano Devices, School of Physics, Renmin University of China, Beijing 100872, China;* orcid.org/0000-0002-8578-366X

**Rui Xu** − *Key Laboratory of Quantum State Construction and Manipulation (Ministry of Education), School of Physics, Renmin University of China, Beijing 100872, China; Beijing Key Laboratory of Optoelectronic Functional Materials & Micro-Nano Devices, School of Physics, Renmin University of China, Beijing 100872, China*

**Li Huang** − *Beijing National Laboratory for Condensed Matter Physics, Institute of Physics, Chinese Academy of Sciences, Beijing 100190, China*

**Wei Ji** − *Key Laboratory of Quantum State Construction and Manipulation (Ministry of Education), School of Physics, Renmin University of China, Beijing 100872, China; Beijing Key Laboratory of Optoelectronic Functional Materials & Micro-Nano Devices, School of Physics, Renmin University of China, Beijing 100872, China;* orcid.org/0000-0001-5249-6624

**Hong-Jun Gao** − *Beijing National Laboratory for Condensed Matter Physics, Institute of Physics, Chinese Academy of Sciences, Beijing 100190, China;* orcid.org/0000-0002-6766-0623

Complete contact information is available at: https://pubs.acs.org/10.1021/acs.jpcc.6c00663


### Author Contributions

[⊥]M.W., C.L., and B.S. contributed equally to this work. L.L., C.P., and Z.C. conceived the research project. M.W. performed the STM experiments and analysis of STM data. C.L., S.M., and X.P. performed the AFM measurements. B.X. grew the



https://doi.org/10.1021/acs.jpcc.6c00663
J. Phys. Chem. C 2026, 130, 6653−6662

single crystals. Y.G., S.M., F.P., R.X., L.H., W.J., and H.G. helped in the experiments. M.W. and Z.C. wrote the manuscript with inputs from all authors.

### Notes

The authors declare no competing financial interest.

## ■ ACKNOWLEDGMENTS

This project was supported by the National Key R&D Program of China (MOST) (Grant Nos. 2023YFA1406500 and 2024YFA1207700), the National Natural Science Foundation of China (NSFC) (Nos. 92477128, 92580137, 92477205, 12374200, 11604063, 11974422, 12104504, 12504203, and 62488201), the Fundamental Research Funds for the Central Universities and the Research Funds of Renmin University of China (No. 21XNLG27), and the High-level Talent Research Start-up Project Funding of Henan Academy of Sciences (Project 20251827003). Y.Y. Geng was supported by the Outstanding Innovative Talents Cultivation Funded Programs 2023 of Renmin University of China. This paper is an outcome of "Two-dimensional anisotropic series of materials $FePd_{2+x}Te_2$: a structural modulation study from the atomic scale to the mesoscopic scale" (RUC25QSDL128), funded by Qiushi Academic Project of Renmin University of China in 2025.

## ■ REFERENCES

(1) Novoselov, K. S.; Geim, A. K.; Morozov, S. V.; Jiang, D.; Zhang, Y.; Dubonos, S. V.; Grigorieva, I. V.; Firsov, A. A. Electric field effect in atomically thin carbon films. *Science* **2004**, *306*, 666−669.

(2) Dong, H.; Li, S.; Mi, S.; Guo, J.; Suonan, Z.; Wu, H.; Geng, Y.; Wang, M.; Xu, H.; Guan, L.; Pang, F.; Ji, W.; Xu, R.; Cheng, Z. Strain-engineered rippling at the bilayer-$MoS_2$ interface identified by advanced atomic force microscopy. *Front. Phys.* **2024**, *19*, No. 63201.

(3) Geng, Y.; Li, C.; Mi, S.; Wang, M.; Han, X.; Hu, H.; Wang, Y.; You, H.; Meng, S.; Wu, H.; Guo, J.; Zhu, S.; Li, Y.; Sugawara, Y.; Hussain, S.; Pang, F.; Rui, X.; Cheng, Z. Unveiling the delicate "hidden" conditions at the interface of 2D materials by multimodal atomic force microscopy. *Front. Phys.* **2025**, *21*, No. 085205.

(4) Geng, Y.; Wang, M.; Meng, S.; Mi, S.; Li, C.; Hu, H.; Guo, J.; Rui, X.; Pang, F.; Ji, W.; Zhou, W.; Cheng, Z. Realization of polytype heterostructures via delicate structural transitions from a doped-Mott insulator. *Chin. Phys. Lett.* **2026**, *43*, No. 030705.

(5) Zhao, J. L.; Ma, D. T.; Wang, C.; Guo, Z. N.; Zhang, B.; Li, J. Q.; Nie, G. H.; Xie, N.; Zhang, H. Recent Advances in Anisotropic Two-Dimensional Materials and Device Applications. *Nano Res.* **2021**, *14*, 897−919.

(6) Gao, Z.-d.; Jiang, Z.; Li, J.; Li, B.; Long, Y.; Li, X.; Yin, J.; Guo, W. Anisotropic Mechanics of 2D Materials. *Adv. Eng. Mater.* **2022**, *24*, No. 2200519.

(7) Li, L.; Han, W.; Pi, L.; Niu, P.; Han, J.; Wang, C.; Su, B.; Li, H.; Xiong, J.; Bando, Y.; Zhai, T. Emerging In-Plane Anisotropic Two-Dimensional Materials. *InfoMat* **2019**, *1*, 54−73.

(8) Chen, C.; Lv, H.; Zhang, P.; Zhuo, Z.; Wang, Y.; Ma, C.; Li, W.; Wang, X.; Feng, B.; Cheng, P.; Wu, X.; Wu, K.; Chen, L. Synthesis of Bilayer Borophene. *Nat. Chem.* **2022**, *14*, 25−31.

(9) Mannix, A. J.; Zhou, X. F.; Kiraly, B.; Wood, J. D.; Alducin, D.; Myers, B. D.; Liu, X.; Fisher, B. L.; Santiago, U.; Guest, J. R.; Yacaman, M. J.; Ponce, A.; Oganov, A. R.; Hersam, M. C.; Guisinger, N. P. Synthesis of Borophenes: Anisotropic, Two-Dimensional Boron Polymorphs. *Science* **2015**, *350*, 1513−1516.

(10) Bishop, G. G.; Graham, A. P.; Minanic, K.; Wendel, J. K.; Hinch, B. J.; Kochanski, G. P. Manifestation of Twofold Anisotropic Domain Growth Kinetics on Fourfold Substrates. *Phys. Rev. Lett.* **1997**, *79*, 1409−1412.

(11) Lu, X.; Chen, Z.; Cao, Y.; Tang, Y.; Xu, R.; Saremi, S.; Zhang, Z.; You, L.; Dong, Y.; Das, S.; Zhang, H.; Zheng, L.; Wu, H.; L, W.; Xie, G.; Liu, X.; Li, J.; Chen, L.; Chen, L.-Q.; Cao, W.; Martin, L. W. Mechanical-Force-Induced Non-Local Collective Ferroelastic Switching in Epitaxial Lead-Titanate Thin Films. *Nat. Commun.* **2019**, *10*, No. 3951.

(12) Chen, X.; Lu, X.; Deng, B.; Sinai, O.; Shao, Y.; Li, C.; Yuan, S.; Tran, V.; Watanabe, K.; Taniguchi, T.; Naveh, D.; Yang, L.; Xia, F. Widely Tunable Black Phosphorus Mid-Infrared Photodetector. *Nat. Commun.* **2017**, *8*, No. 1672.

(13) Tian, Z.; Guo, C.; Zhao, M.; Li, R.; Xue, J. Two-Dimensional SnS: A Phosphorene Analogue with Strong In-Plane Electronic Anisotropy. *ACS Nano* **2017**, *11*, 2219−2226.

(14) Xia, F.; Wang, H.; Jia, Y. Rediscovering black phosphorus as an anisotropic layered material for optoelectronics and electronics. *Nat. Commun.* **2014**, *5*, No. 4458.

(15) Luo, Z.; Maassen, J.; Deng, Y.; Du, Y.; Garrelts, R. P.; Lundstrom, M. S.; Ye, P. D.; Xu, X. Anisotropic in-plane thermal conductivity observed in few-layer black phosphorus. *Nat. Commun.* **2015**, *6*, No. 8572.

(16) Zhao, L. D.; Lo, S. H.; Zhang, Y.; Sun, H.; Tan, G.; Uher, C.; Wolverton, C.; Dravid, V. P.; Kanatzidis, M. G. Ultralow Thermal Conductivity and High Thermoelectric Figure of Merit in SnSe Crystals. *Nature* **2014**, *508*, 373−377.

(17) Burch, K. S.; Mandrus, D.; Park, J.-G. Magnetism in Two-Dimensional van Der Waals Materials. *Nature* **2018**, *563*, 47−52.

(18) Gong, C.; Li, L.; Li, Z.; Ji, H.; Stern, A.; Xia, Y.; Cao, T.; Bao, W.; Wang, C.; Wang, Y.; Qiu, Z. Q.; Cava, R. J.; Louie, S. G.; Xia, J.; Zhang, X. Discovery of Intrinsic Ferromagnetism in Two-Dimensional van der Waals Crystals. *Nature* **2017**, *546*, 265−269.

(19) Huang, B.; Clark, G.; Navarro-Moratalla, E.; Klein, D. R.; Cheng, R.; Seyler, K. L.; Zhong, D.; Schmidgall, E.; McGuire, M. A.; Cobden, D. H.; Yao, W.; Xiao, D.; Jarillo-Herrero, P.; Xu, X. Layer-dependent ferromagnetism in a van der Waals crystal down to the monolayer limit. *Nature* **2017**, *546*, 270−273.

(20) Jiang, S.; Li, L.; Wang, Z.; Mak, K. F.; Shan, J. Controlling magnetism in 2D $CrI_3$ by electrostatic doping. *Nat. Nanotechnol.* **2018**, *13*, 549−553.

(21) Deng, Y.; Yu, Y.; Song, Y.; Zhang, J.; Wang, N. Z.; Sun, Z.; Yi, Y.; Wu, Y. Z.; Wu, S.; Zhu, J.; Wang, J.; Chen, X. H.; Zhang, Y. Gate-tunable room-temperature ferromagnetism in two-dimensional $Fe_3GeTe_2$. *Nature* **2018**, *563*, 94−99.

(22) May, A. F.; Ovchinnikov, D.; Zheng, Q.; Hermann, R.; Calder, S.; Huang, B.; Fei, Z.; Liu, Y.; Xu, X.; McGuire, M. A. Ferromagnetism Near Room Temperature in the Cleavable van Der Waals Crystal Fe5GeTe2. *ACS Nano* **2019**, *13*, 4436−4442.

(23) Tian, S.; Zhang, J.-F.; Li, C.; Ying, T.; Li, S.; Zhang, X.; Liu, K.; Lei, H. Ferromagnetic van Der Waals Crystal $VI_3$. *J. Am. Chem. Soc.* **2019**, *141*, 5326−5333.

(24) Zhang, G.; Guo, F.; Wu, H.; Wen, X.; Yang, L.; Jin, W.; Zhang, W.; Chang, H. Above-room-temperature strong intrinsic ferromagnetism in 2D van der Waals Fe3GaTe2 with large perpendicular magnetic anisotropy. *Nat. Commun.* **2022**, *13*, No. 5067.

(25) Tian, C.; Pan, F.; Xu, S.; Ai, K.; Xia, T.; Cheng, P. Tunable magnetic properties in van der Waals crystals $(Fe_{1-x}Co_x)_5GeTe_2$. *Appl. Phys. Lett.* **2020**, *116*, No. 202402.

(26) Wu, H.; Guo, J.; Zhaxi, S.; Xu, H.; Mi, S.; Wang, L.; Chen, S.; Xu, R.; Ji, W.; Cheng, Z.; Pang, F. Controllable CVD-Growth of 2D $Cr_5Te_8$ Nanosheets with Thickness-Dependent Magnetic Domains. *ACS Appl. Mater. Interfaces* **2023**, *15*, 26148−26158.

(27) Cai, X.; Song, T.; Wilson, N. P.; Clark, G.; He, M.; Zhang, X.; Taniguchi, T.; Watanabe, K.; Yao, W.; Xiao, D.; McGuire, M. A.; Cobden, D. H.; Xu, X. Atomically Thin $CrCl_3$: An In-Plane Layered Antiferromagnetic Insulator. *Nano Lett.* **2019**, *19*, 3993−3998.

(28) Wang, Z.; Gibertini, M.; Dumcenco, D.; Taniguchi, T.; Watanabe, K.; Giannini, E.; Morpurgo, A. F. Determining the Phase Diagram of Atomically Thin Layered Antiferromagnet $CrCl_3$. *Nat. Nanotechnol.* **2019**, *14*, 1116−1122.

(29) Bedoya-Pinto, A.; Ji, J.-R.; Pandeya, A. K.; Gargiani, P.; Valvidares, M.; Sessi, P.; Taylor, J. M.; Radu, F.; Chang, K.; Parkin, S.



https://doi.org/10.1021/acs.jpcc.6c00663
J. Phys. Chem. C 2026, 130, 6653−6662

S. P. Intrinsic 2D-XY Ferromagnetism in a van der Waals Monolayer. *Science* **2021**, *374*, 616−620.
(30) Telford, E. J.; Dismukes, A. H.; Lee, K.; Cheng, M.; Wieteska, A.; Bartholomew, A. K.; Chen, Y. S.; Xu, X.; Pasupathy, A. N.; Zhu, X.; Dean, C. R.; Roy, X. Layered Antiferromagnetism Induces Large Negative Magnetoresistance in the van der Waals Semiconductor CrSBr. *Adv. Mater.* **2020**, *32*, No. 2003240.
(31) Telford, E. J.; Dismukes, A. H.; Dudley, R. L.; Wiscons, R. A.; Lee, K.; Chica, D. G.; Ziebel, M. E.; Han, M. G.; Yu, J.; Shabani, S.; Scheie, A.; Watanabe, K.; Taniguchi, T.; Xiao, D.; Zhu, Y.; Pasupathy, A. N.; Nuckolls, C.; Zhu, X.; Dean, C. R.; Roy, X. Coupling between magnetic order and charge transport in a two-dimensional magnetic semiconductor. *Nat. Mater.* **2022**, *21*, 754−760.
(32) Boix-Constant, C.; Jenkins, S.; Rama-Eiroa, R.; Santos, E. J. G.; Mañas-Valero, S.; Coronado, E. Multistep magnetization switching in orthogonally twisted ferromagnetic monolayers. *Nat. Mater.* **2024**, *23*, 212−218.
(33) Shi, B.; Geng, Y.; Wang, H.; Yang, J.; Shang, C.; Wang, M.; Mi, S.; Huang, J.; Pan, F.; Gui, X.; Wang, J.; Liu, J.; Xu, D.; Zhang, H.; Qin, J.; Wang, H.; Hao, L.; Tian, M.; Cheng, Z.; Zheng, G.; Cheng, P. $FePd_2Te_2$: An Anisotropic Two-Dimensional Ferromagnet with One-Dimensional Fe Chains. *J. Am. Chem. Soc.* **2024**, *146*, 21546−21554.
(34) Chen, Z.; Yang, Y.; Guo, J.-G. Fourfold Anisotropic Magnetoresistance and Unconventional Critical Exponents in Twinned FePd2Te2. 2024, arXiv:physics/2411.15842. arXiv.org e-Print archive. https://arxiv.org/abs/2411.15842.
(35) Mi, S.; Wang, M.; Shi, B.; Li, S.; Pei, X.; Geng, Y.; Meng, S.; Xu, R.; Huang, L.; Ji, W.; Pang, F.; Cheng, P.; Guo, J.; Cheng, Z. Atomic-to-Mesoscale Twinning Effects and Strain-Driven Magnetic States in an Anisotropic 2D Ferromagnet $FePd_2Te_2$. *ACS Nano* **2025**, *19*, 34318−34328.
(36) Zhang, J.; Shi, B.; Xu, H.; Song, Y.; Zou, Y.; Li, Z.; Dai, H.; Song, Y.; Jin, Q.; Cheng, P.; Jin, Z.; Zhang, Z. Enhanced THz Emission and Chirality Control in van der Waals Ferromagnetic $FePd_2Te_2$/Pt Heterostructures. *J. Am. Chem. Soc.* **2025**, *147*, 19878−19885.
(37) Penacchio, R. F. S.; Mohamed, S.; Morelhao, S. L.; Bud'ko, S. L.; Canfield, P. C.; Slade, T. J. Structural phase transitions in the van der Waals ferromagnets FexPdyTe2. 2024, arXiv:physics/2511.15584. arXiv.org e-Print archive. https://arxiv.org/abs/2511.15584.
(38) Cao, X.; Liu, Y.; Ma, X.; Gao, X.; Andreeva, T.; Zhang, F. Electronic structure and optoelectronic properties of $MoS_2/FePd_2Te_2$ heterojunction based on first principles. *Chem. Phys. Lett.* **2025**, *878*, No. 142317.
(39) Li, Y.; Liao, J.; Ma, J.; Zhang, Y.; Li, T.; Wang, J.; Wang, H.; Guo, H.; Dai, J.; Li, Y. Anomalous Hall and Nernst Effects in the Two-Dimensional Ferromagnetic Metal $FePd_2Te_2$. *Solid State Sci.* **2025**, *168*, No. 108044.
(40) Ruiz, A. M.; Shumilin, A.; Dey, S.; Lopez-Alcala, D.; Baldovi, J. J. Tunable Itinerant Ferromagnetism in the Two-Dimensional FePd2Te2 Hosting 1D Spin Chains. 2025, arXiv:physics/2506.01009. arXiv.org e-Print archive. https://arxiv.org/abs/2506.01009. DOI: 10.48550/arXiv.2506.01009.




https://doi.org/10.1021/acs.jpcc.6c00663
J. Phys. Chem. C 2026, 130, 6653−6662